CHALMERS
UNIVERSITY OF TECHNOLOGY

Development of yttria-stabilized zirconia and graphene coatings obtained by suspension plasma spraying: Thermal stability and influence on

Ceramics International xxx (xxxx) xxx

Contents lists available at ScienceDirect

Ceramics International

journal homepage: www.elsevier.com/locate/ceramint

Development of yttria-stabilized zirconia and graphene coatings obtained by suspension plasma spraying: Thermal stability and influence on mechanical properties

Antonio Mulone [a,*], Satyapal Mahade [b], Stefan Björklund [b], Dennis Lundström [c], Björn Kjellman [c], Shrikant Joshi [b], Uta Klement [a]

[a] Chalmers University of Technology, Department of Industrial and Materials Science, Gothenburg, Sweden
[b] University West, Department of Engineering Science, Trollhättan, Sweden
[c] GKN Aerospace Engines Sweden, Trollhättan, Sweden

ARTICLE INFO

Keywords:
Graphene
Suspension plasma spray
Yttria stabilized zirconia
Microstructure
Raman
Heat treatment

ABSTRACT

This study investigated the feasibility of depositing graphene nanoplatelet (GNP)-reinforced yttria-stabilized zirconia (YSZ) composite coatings. The coatings were deposited from an ethanol-based mixed YSZ and GNP suspension using suspension plasma spraying (SPS). Raman spectroscopy confirmed the presence of GNPs in the YSZ matrix, and scanning electron microscopy (SEM) analysis revealed a desired columnar microstructure with GNPs distributed predominantly in the inter-columnar spacing of the YSZ matrix. The as-deposited YSZ-GNP coatings were subjected to different isothermal treatments—400, 500, and 600 °C for 8 h—to study the thermal stability of the GNPs in the composite coatings. Raman analysis showed the retention of GNPs in specimens exposed to temperatures up to 500 °C, although the defect concentration in the graphitic structure increased with increasing temperature. Only a marginal effect on the mechanical properties (i.e., hardness and fracture toughness) was observed for the isothermally treated coatings.

1. Introduction

In recent years, graphene and related graphene-related compounds, such as graphene nanoplatelets (GNPs) and graphene oxide (GO), have been extensively studied because of their outstanding mechanical [1], corrosion-resistant [2], electrical [3] and thermal [4] properties. Owing to its stacked planar structure, graphene is considered an excellent solid lubricant [5]. While the carbon atoms forming the 2D monolayers are linked via strong covalent bonds, the weaker van der Waals forces between adjacent graphene layers in GNPs allow the different layers to slide easily [6]. To exploit the excellent properties mentioned above, significant efforts from the scientific community have focused on manufacturing of graphene-containing composites [7–9]. In particular, owing to its superior mechanical properties (e.g., Young's modulus of 1 TPa and flexural strength of 42 N/m [10]), graphene is considered a promising reinforcement for monolithic ceramics. For example, as reported by Walker et al. [11] the incorporation of 1–5 vol% of graphene resulted in an increase of approximately 235% in the fracture toughness of a Si_3N_4 matrix. Liu et al. [12] obtained a ~40% increase in the fracture toughness of spark plasma sintered zirconia-toughened alumina reinforced with 0.8 vol% graphene platelets, whereas a 53% increase was reported by Wang et al. [13] in graphene-alumina composites obtained via colloidal processing. Such impressive increases in toughness have been related to the ability of GNPs to deflect cracks and achieve crack-bridging [14,15]. The ability to obtain such tough ceramic composites by adding graphene is of significant interest for various transportation, aerospace, and military applications [16,17]. However, despite the studies on the beneficial influence of graphene and GNPs on the strength of ceramic composites, other studies have also reported a decrease in the hardness with the addition of GNPs compared to monolithic ceramics [18,19]. Other studies have reported a decrease in hardness only after increasing the GNP content above a certain threshold [20,21]. In these studies, the increase in the hardness of the composite containing a low amount of GNPs was related to GNP-induced grain refinement [21], whereas the decrease in hardness for higher GNP contents was related to the softer nature of GNPs [22] as compared to monolithic ceramics and induced grain slipping [23].

Previous studies have mainly investigated sintering routes to obtain

* Corresponding author.
E-mail address: mulone@chalmers.se (A. Mulone).

https://doi.org/10.1016/j.ceramint.2022.11.055
Received 20 June 2022; Received in revised form 26 October 2022; Accepted 3 November 2022
Available online 7 November 2022

Table 1
SPS process parameters used to deposit YSZ-GNP composite coatings.

Parameter	Suspension feed (ml/min)	Nozzle (inch)	Gas flow (l/min)	Current (A)	Standoff Distance (mm)	Power (kW)	Enthalpy (kJ/l)	Atomizing gas (l/min)
Composite	100	3/8	300	200	100	121	11,5	20

graphene-ceramic composites, such as spark plasma sintering [11,24] and high-frequency induction heat sintering [21,25]. Such sintering routes are used to sinter ceramics in a vacuum or protective atmosphere and at relatively low temperatures to prevent graphene degradation. Graphene degradation in air can occur at temperatures ≥600 °C [26]. In addition to bulk manufacturing processes, the possibility of producing graphene-ceramic composites as coatings on engineering substrates has recently gained scientific interest [27]. Thermal spraying is an attractive and widely used manufacturing process for depositing large-area protective coatings [28]. To date, limited studies have been conducted on graphene-containing coatings obtained by high-temperature spraying processes, such as thermal spraying, because of the intrinsic risk of graphene degradation during spraying. Despite these challenges, Murray et al. [29] deposited alumina coatings with 1 wt% GNPs utilizing suspension high-velocity oxy-fuel process (S-HVOF) and showed that the GNPs were retained in the coating, with only a slight increase in the defect density of the GNPs structure observed after spraying. An increase in the defectiveness of graphene can result in a decrease in its mechanical properties (e.g. Young's modulus and tensile strength) [30]. Nevertheless, despite the increase in defects, adding GNPs to the alumina matrix reduced the wear rate by two orders of magnitude [29]. Venturi et al. [31] also employed S-HVOF to deposit chromia coatings with 0.2 wt% of GNPs. The addition of such a low quantity of GNPs resulted in improvements in the wear resistance of composite coatings, with a 17% decrease in the friction coefficient. Furthermore, Ganvir et al. [32] and Mahade et al. [33] have also shown that graphene can be retained by employing axial suspension plasma spray (A-SPS) despite the high plasma plume temperature if the deposition conditions are suitably controlled.

Research on GNP-containing coatings obtained by thermal spraying has mostly focused on the feasibility of the spraying process to retain GNPs in a suitable matrix and on the characterization of composite properties. The influence of SPS on the distribution of GNPs has often been overlooked. Therefore, in this study, the authors investigated the possibility of incorporating GNPs into columnar YSZ coatings and the distribution of GNPs within the columnar microstructure. Furthermore, the as-deposited YSZ-GNP coatings were subjected to isothermal treatment for 8 h at various temperatures (400, 500, and 600 °C) to study the thermal stability of the GNPs in the composite coatings. The results presented in this paper open new possibilities for thermally sprayed graphene-containing coatings for use in various functional applications.

2. Experimental

2.1. Coating preparation

Disc-shaped (1 inch diameter × 6 mm thickness) and rectangular (50 mm × 30 mm × 6 mm) Hastelloy-X specimens were used as substrates. A 120-μm-thick bond coat of Ni23.1Co20Cr8.5AlY (AMDRY 386–0, Oerlikon Metco) was deposited on the Hastelloy-X substrates using a high-velocity air fuel (HVAF) process utilizing an M3 (UniqueCoat, US) torch. The substrates were obtained from Haynes International, Ltd. (Manchester, Great Britain). For the top coat, commercial, ethanol-based 8 wt% YSZ suspension (AuerCoat®YSZ, Treibacher Industrie AG, Austria) comprising a solid load of 25 wt% with particle size distribution of D_{50} = 500 nm was used. Commercially available GNPs (AB 304022, abcr GmbH, Germany) of 6–8 nm thickness and a lateral size of 5 μm were used to prepare a mixed YSZ-GNP suspension comprising 5 wt % of GNP relative to the overall solid content. The mixed suspension was placed on rollers for 48 h before spraying. The rolling apparatus was developed in-house by PTC Innovation AB (Trollhättan, Sweden). The cans containing the suspension were placed on rollers, and the apparatus was operated at 100 rpm. An Axial III plasma torch and Nanofeed 350 suspension feeding system from Northwest Mettech Corporation (Vancouver, Canada) were used to deposit the GNP-containing YSZ composite coating. Previously developed SPS parameters that resulted in a columnar microstructure were utilized to deposit the YSZ + GNP composite coating (see Table 1 [34].

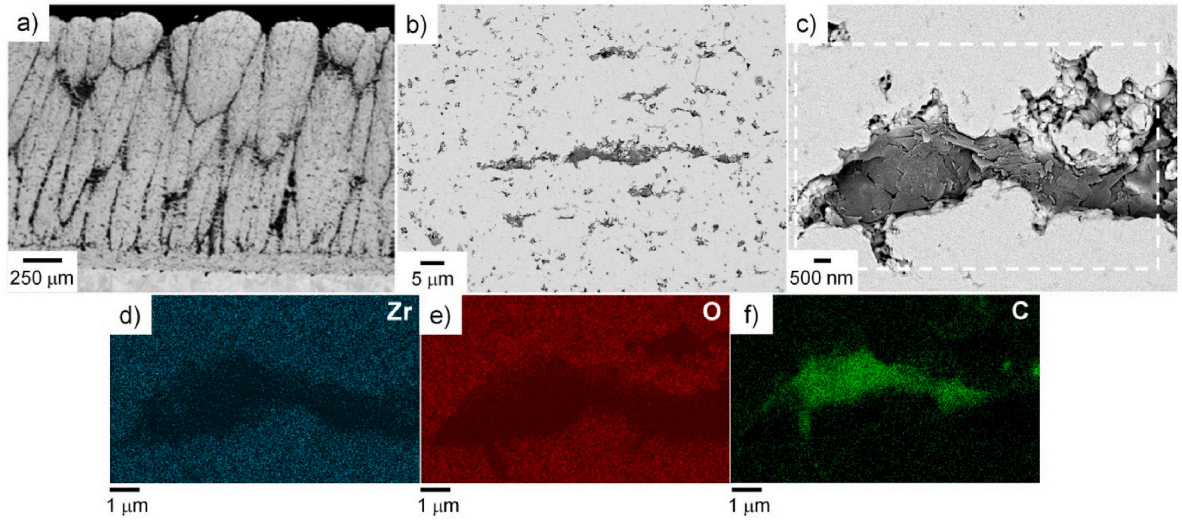

Fig. 1. Backscattered electron (BSE) micrographs showing the columnar microstructure of as-deposited YSZ-GNP coating (a) and revealing GNPs contained in the pores of the YSZ matrix (b and c). EDS mapping was performed in the area highlighted with a dashed box in (c) and the selected elemental maps of zirconium, oxygen, and carbon are included in (d), (e), and (f), respectively.

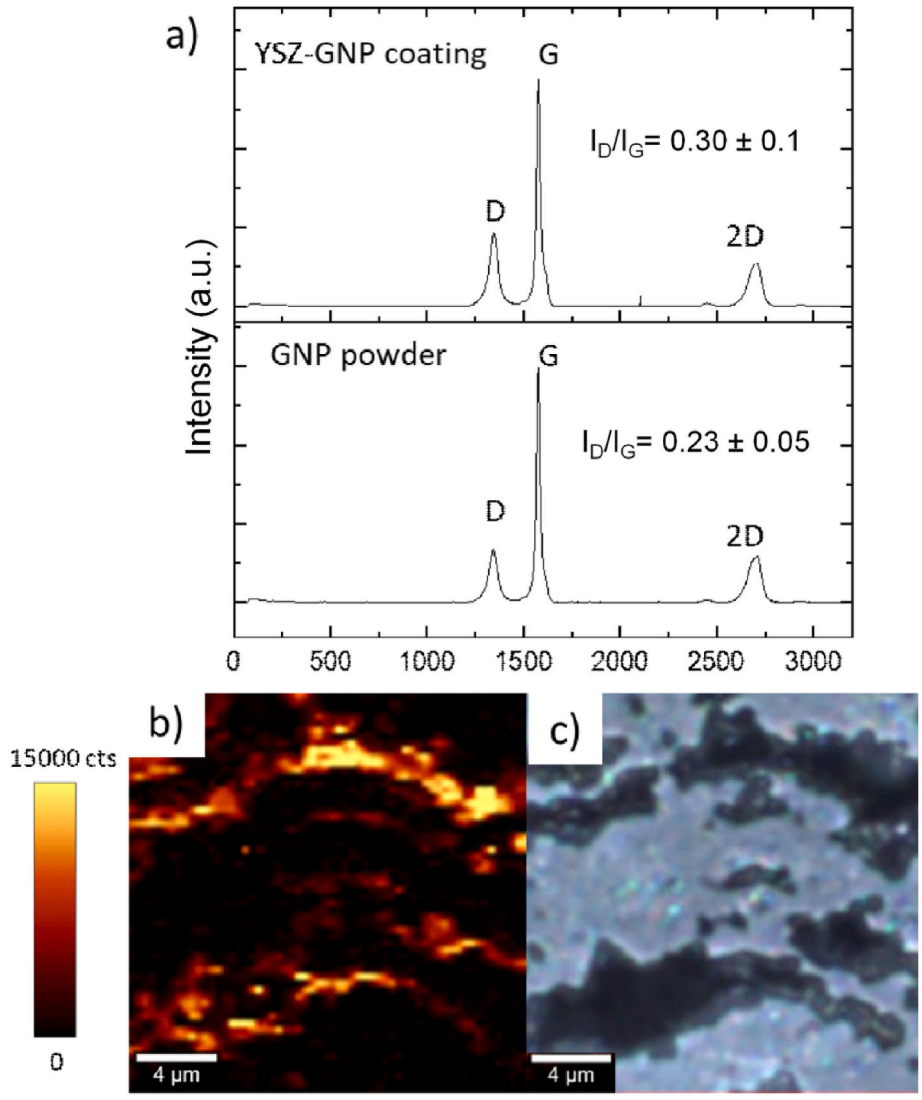

Fig. 2. Representative Raman spectra measured from the GNP feedstock and the YSZ-GNP coating (a) and G band intensity map (b) acquired from the polished cross-section of the composite coating (c). The G band intensity map shows the variation of the G band intensity as a function of the spatial location.

2.2. Coating characterization

The surface morphology and cross-sections of the YSZ-GNP composite coatings were analyzed using a Zeiss Gemini SEM 450 (Zeiss, Oberkochen, Germany). The composite coatings were heat-treated in a Heraeus muffle furnace, keeping the samples at 400, 500, and 600 °C for 8 h under an air atmosphere. After heat treatment, the samples were cooled to room temperature (i.e., 25 °C) inside the furnace. Studying the thermal stability of the GNPs in the composite coating is one of the goals of this study. Hence, the selected temperatures for the isothermal treatment were not related to a specific application but were selected according to the reported temperature at which GNPs combust in air, i.e., 500–600 °C [35]. The cross-sections of the as-deposited composite coatings were prepared using a standard metallographic procedure reported elsewhere [33,36]. The fracture surfaces of the YSZ-GNP coatings were also analyzed. Fracturing of the composite coatings was achieved by sectioning the samples using an IsoMeth High-Speed Pro Precision cutter (Bruheler, Leinfelden-Echterdingen, Germany). Cutting the composite coating at a fast cutting speed (i.e., 10,000 rpm) resulted in the fracturing and pull-off of the YSZ columns. The porosity contents of the as-deposited and isothermally treated composite coatings were analyzed using twenty-five independent cross-sectional SEM micrographs (2000× magnification) acquired from the polished cross-sections of the composites using ImageJ software. Micro-indentation tests were performed on the cross sections of the as-deposited and isothermally treated coatings using an HMV-2 series semi-automatic hardness tester (SHIMADZU Corp., Japan). A square pyramidal diamond indenter is used. A normal load of 0.1 N was applied for the hardness measurements, while a higher load of 1 N was applied for the fracture toughness measurements to generate cracks at the indentation vertices. The fracture toughness of the coatings was calculated using Eq. (1) [37]:

$$KIC = 0.16 * \left(\frac{c}{a}\right)^{-1.5} * \left(H * a^{0.5}\right) \quad (1)$$

where *KIC* denotes the fracture toughness, '*c*' denotes the crack length (in µm), '*a*' is the length of the half diagonal (in µm), and '*H*' represents the hardness of the coating.

3. Results and discussions

3.1. Structural characterization of as-deposited YSZ + GNP coatings

SEM imaging was performed on the polished cross-section of the coating to reveal the microstructure of the as-deposited YSZ-GNP

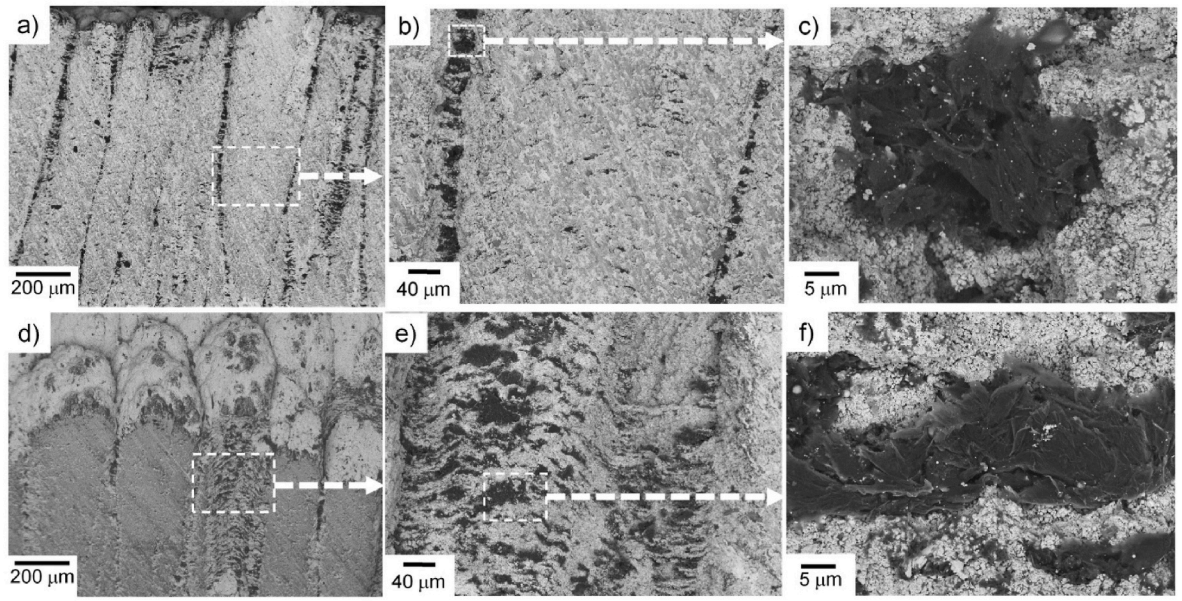

Fig. 3. Backscattered electron (BSE) micrographs acquired from the cross-section of the as-deposited YSZ-GNP coating showing agglomeration of GNPs in the inter-columnar spacing of the YSZ matrix (a–c). GNP agglomeration in the inter-columnar region is more clearly revealed in micrographs of a fractured YSZ column (d–f) acquired by tilting the SEM stage of 30 °.

coatings. As shown in Fig. 1a, the composite coating had a thickness of 1590 ± 30 μm and a columnar structure with columns of ~200 μm in width. Backscattered electron (BSE) imaging of the intra-columnar region of the composite revealed the presence of relatively fine pores, appearing in black in Fig. 1b, as well as elongated (horizontal) pores that appear to contain a dark grey phase. The grey phase is characterized by a fine platelet-like structure, as shown in Fig. 1c, which is rich in carbon, as revealed by the EDS analysis shown in Fig. 1f. These results strongly suggest that the observed phase consisted of the co-sprayed GNPs. Previous studies have also suggested the presence of GNPs in the pores of thermally sprayed coatings [38]. Thus, it can be assumed that GNPs are responsible for pore formation in composite coatings, with the bonding between successive YSZ spalts prevented by the presence of GNPs [39].

Raman measurements were performed on the polished cross-section to confirm the presence of GNPs in the pores of the YSZ-GNP composite and to determine the influence of the spraying process on the GNP structure. Fig. 2a shows a comparison of the representative Raman spectra acquired from the YSZ-GNP composite and GNPs used as the starting feedstock. The Raman spectra from the composite coating and the GNPs both show the characteristic peaks expected from the GNPs: the D band at 1350 cm^{-1}, G band at 1579 cm^{-1}, and 2D band at 2705 cm^{-1} [35,40]. Generally, the I_D/I_G ratio can provide a good indication of the defectiveness of graphene-related materials [29,40]. Hence, from the analysis of the I_D/I_G ratio, it was possible to estimate the number of defects introduced in the GNPs structure during the spraying process. Essentially, the G band is related to the stretching of sp^2 hybridized carbon bonds, whereas the D band arises due to the incorporation of defects (e.g., substitutional atoms) in the hexagonal carbon lattice [41]. The I_D/I_G ratio, shown in Fig. 2a, was obtained as an average from a minimum of five measurements acquired at different locations. The limited slight increase which is observed for the composite coating (from $I_D/I_G = 0.23 \pm 0.05$ for the GNP powder to $I_D/I_G = 0.3 \pm 0.1$ for the composite) confirms that the GNPs have largely preserved their structural integrity upon spraying with only a minor increase in their defect density. Thus, a highly defective graphene layer can result in an I_D/I_G ratio as high as three [40].

Raman mapping of the polished cross-section of the composite coatings was also performed to analyze the distribution of GNPs within the YSZ columns. Fig. 2b shows the G-band intensity map, and Fig. 2c shows its acquisition site. The G-band map highlights the variation in the intensity of the G-band as a function of the spatial location. Therefore, the bright areas on the map indicate the presence of GNPs, whereas the dark areas indicate the absence of GNPs. As shown in Fig. 2b, GNPs can be observed within the elongated pores/cavities present in the YSZ columns, which appear dark in Fig. 2c. These results confirm that the dark grey phase observed within the YSZ matrix in Fig. 1 corresponds to GNPs. In addition, the larger GNP-rich areas observed in Fig. 2b have a lateral size of approximately 5–15 μm, which is comparable to the initial GNP feedstock lateral size (i.e., ~5 μm). The SPS of a mixed YSZ-GNP suspension proved to be suitable for obtaining a GNP-containing YSZ composite and showed that the GNPs survived the spraying process with minimal structural changes.

However, GNPs were not only observed in the YSZ columns. As revealed from the SEM micrographs in Fig. 3 a-c, GNPs appeared to accumulate in large quantities in the inter-columnar spacing of the YSZ matrix. This is more evident from the images of the fracture surfaces along the cross-section of the composite coatings. As shown in Fig. 3d, fracturing resulted in the pull-out of the entire YSZ column, which revealed the inter-columnar area, as shown in Fig. 3e. Here, a larger quantity of GNPs is clearly seen compared to the GNPs found in the intra-columnar area (see comparison between Fig. 3b and e). In addition, in the inter-columnar region, larger GNPs agglomerates, that is, around 30–40 μm, were observed (see Fig. 3c and f) as compared to the agglomerates observed within the YSZ columns (see Figs. 1c and 2c). These observations suggest that upon spraying, the GNPs have a higher tendency to agglomerate in the inter-columnar region rather than within the YSZ columns.

Such agglomeration of GNPs can be related to the processing challenges when depositing GNP-containing composites. During processing, GNPs can easily re-stack and agglomerate owing to strong van der Waals forces and the interaction between electrons in the π orbitals [42].

It can be hypothesized that the mechanism resulting in the preferential agglomeration of the GNPs in the inter-columnar spacing is probably related to the columnar growth mechanism during spraying. The formation of a columnar microstructure in YSZ coatings obtained via SPS is mainly related to two mechanisms that have already been described in the literature: (i) the equilibrium between the drag force (F_D) and adhesion force (F_A) on the powder particles sprayed on the

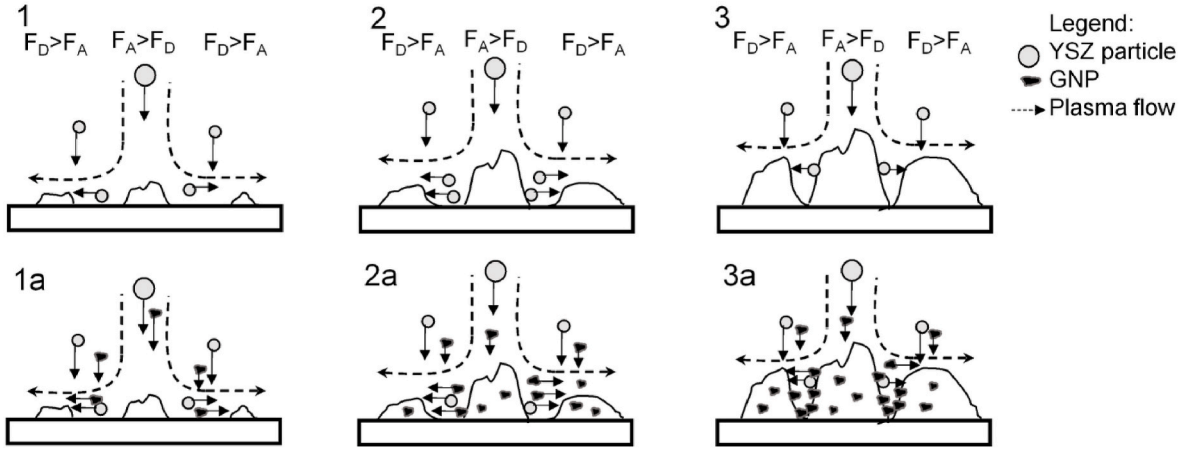

Fig. 4. Schematic illustration of the columnar growth mechanism in YSZ coatings (1, 2, and 3). The same mechanism is considered to be responsible for GNPs agglomeration in the inter-columnar region upon spraying a mixed YSZ-GNP suspension (1a, 2a, and 3a). Step 1: formation of single splats irregularly distributed. Step 2: YSZ particle trajectory determined by equilibrium of forces and particle sizes. Step 3: continuous columnar growth. Schematic illustration inspired by Ref. [45].

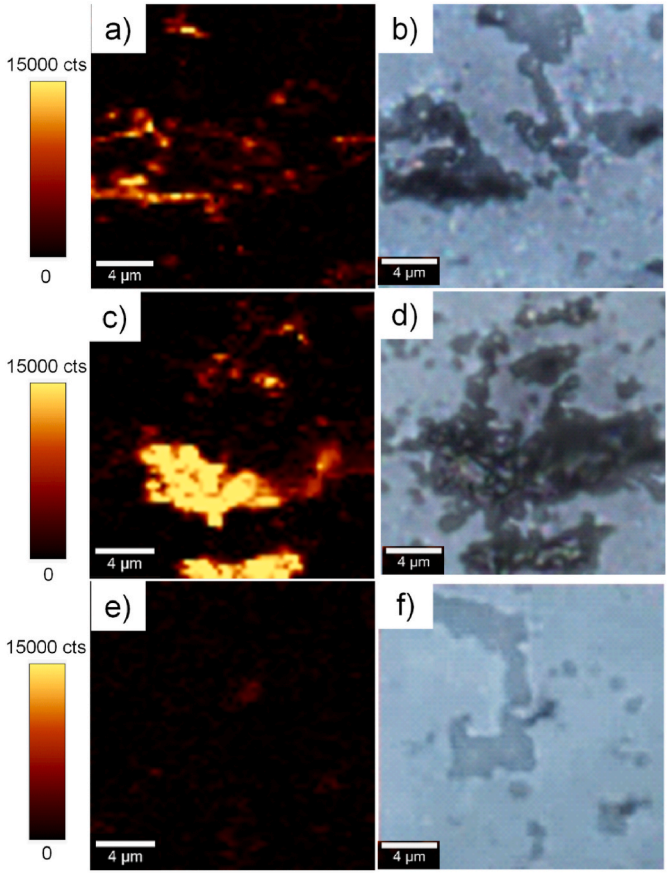

Fig. 5. G band intensity map and its acquisition area in the polished cross-sections of the heat-treated coatings at 400 °C (a and b), 500 °C (c and d), and 600 °C (e and f).

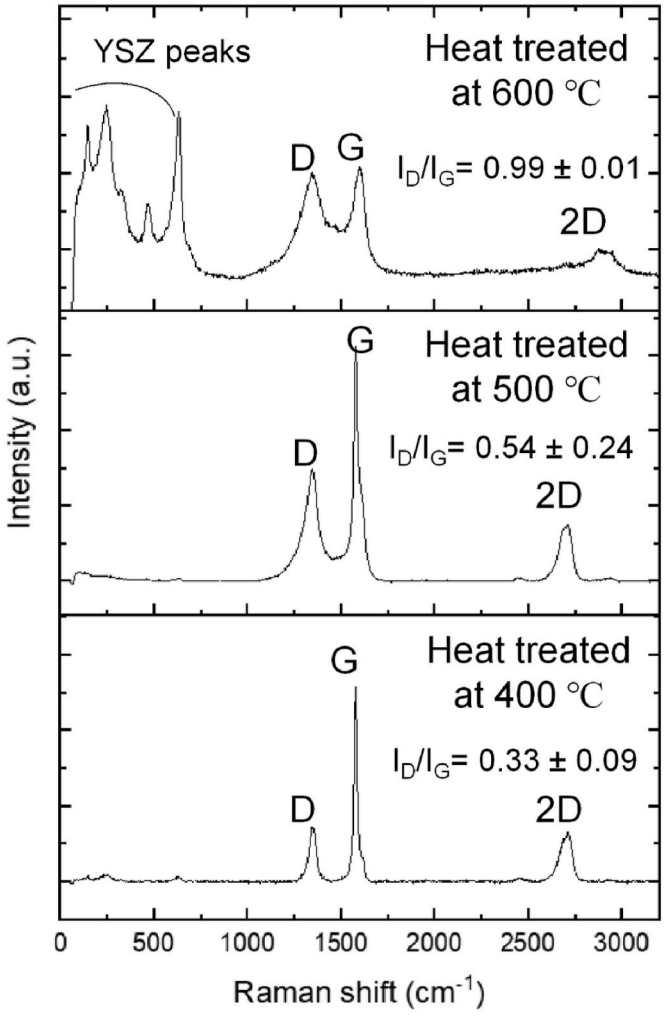

Fig. 6. Representative Raman spectra obtained from the heat-treated YSZ-GNP coatings.

substrates [43] and (ii) the so-called "shadowing effect" [44]. In the first mechanism, the dimensions and density of the sprayed particles play important roles. For larger particles transported close to the axis of the plasma jet, the relation $F_A \geq F_D$ holds. However, for smaller and lighter particles, there is a different balance of forces, that is, $F_D \geq F_A$, which causes them to move perpendicular to the jet axis and adhere to protrusions on their way. This mechanism results in the formation of a columnar microstructure even in the presence of a smooth substrate [45]. Therefore, it is reasonable to assume that upon spraying the mixed YSZ-GNP suspension, the smaller and lighter GNPs are mainly affected

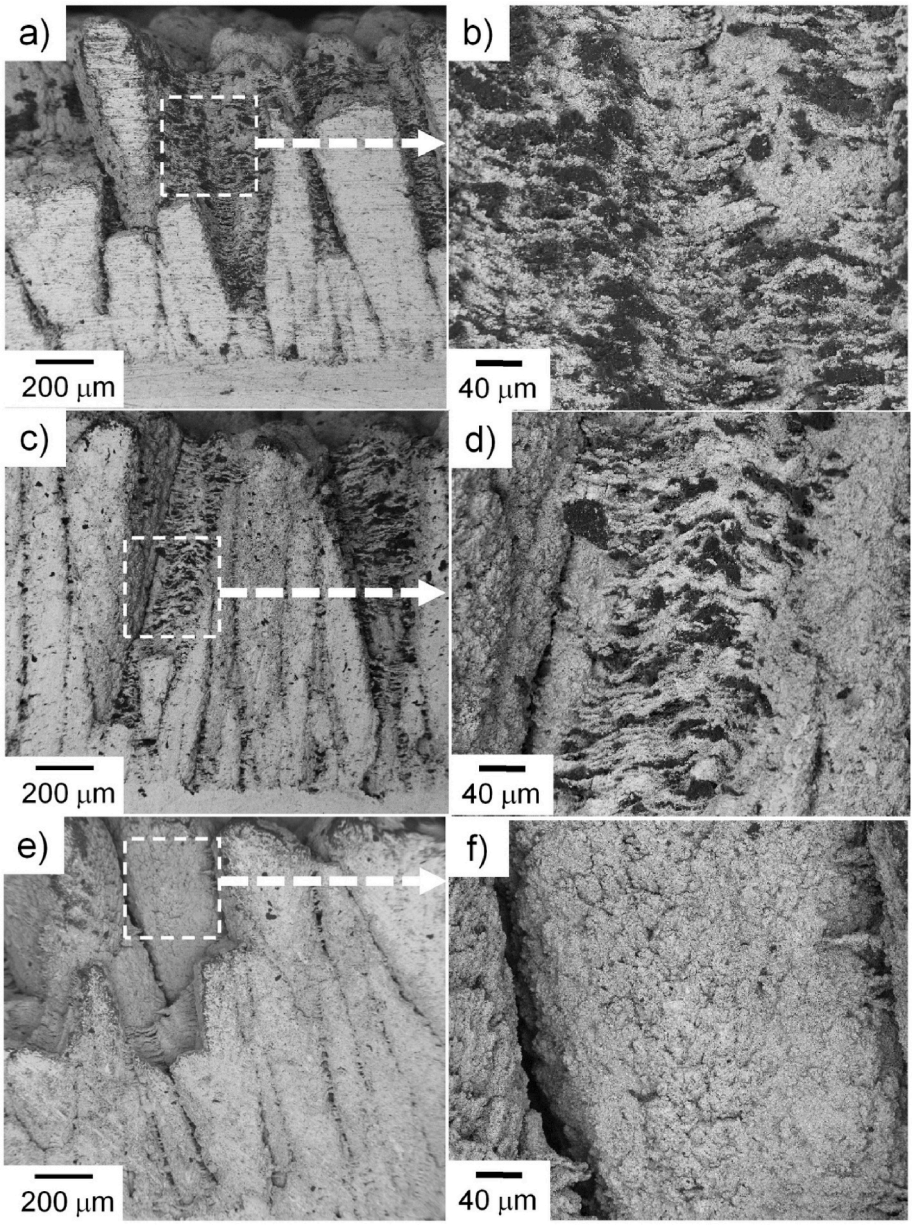

Fig. 7. Inter-columnar regions revealed after fracturing and pulling out parts of a YSZ column of the composite coating heat treated at 400 °C (a–b), 500 °C (c–d), and 600 °C (e–f).

by the drag force. This causes a higher agglomeration of the GNPs at the sides of the growing YSZ columns, and thus in the resulting inter-columnar region of the sprayed YSZ-GNP coatings. A schematic illustration of the mechanism responsible for columnar growth and agglomeration of GNPs in the inter-columnar spacing is shown in Fig. 4.

The results presented show the role of the YSZ microstructure in the resulting distribution of GNPs. Suspension plasma spraying offers the possibility of obtaining various microstructures by changing different spraying parameters (e.g., particle size, powder concentration in suspension, and type of solvent [45]). Therefore, changing the distribution of GNPs by varying the coating microstructure can provide opportunities for thermally sprayed graphene-containing coatings to be used in various functional applications.

3.2. Structural characterization of heat-treated YSZ-GNP coatings

Raman analysis was used to examine the thermal stability of GNPs in the composite coatings subjected to heat treatment. Fig. 5 shows the Raman maps obtained from the polished cross-sections of the heat-treated coatings, while Fig. 6 shows the representative Raman spectra. As shown in Fig. 5, the GNPs were retained in the composite coatings even after heat treatment at 400 and 500 °C. In fact, similar to the as-deposited sample, the G band Raman map shows areas characterized by a high G peak intensity (appearing bright) in the proximity of pores in the YSZ matrix (compare Fig. 5a and b). However, after heat treatment, an increase in the defect density of the GNPs was observed, as shown by the progressive increase in the average I_D/I_G ratio with exposure temperature in Fig. 6 ($I_D/I_G = 0.33 \pm 0.09$ after heat treatment at 400 °C, and $I_D/I_G = 0.54 \pm 0.24$ after heat treatment at 500 °C). Such an increase in the defect density of the GNPs can be expected owing to oxygen pickup upon annealing, as previously reported [46]. After heat treatment at 600 °C, the GNPs appeared to be significantly affected by annealing. As shown in the Raman map in Fig. 5e, only small areas are characterized by the presence of the G peak.

Furthermore, the measured intensity of the G peak in the coating heat-treated at 600 °C was significantly lower than that of the composite

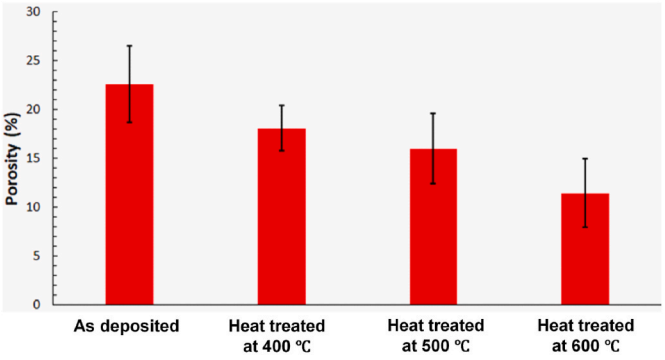

Fig. 8. Porosity content in as-deposited and heat-treated YSZ-GNP coatings.

coatings annealed at lower temperatures. The structural changes occurring in the GNPs were more clearly discernible from the representative Raman spectra shown in Fig. 6. Here, the intensity of the D peak was further increased, resulting in an average I_D/I_G ratio of approximately 1 for the coating heat treated at 600 °C. Such a high I_D/I_G ratio can, for example, be assumed to be associated with the presence of graphene oxide [14]. Thermogravimetry (TG) analysis of GNPs under air atmosphere has shown that combustion of GNPs occurs at temperatures between 550 and 750 °C [35]. The progressive oxidation and combustion of the GNPs was also suggested by the SEM images, where far fewer GNPs were observed in the fractured cross-sections of the heat-treated coatings, see Fig. 7.

3.3. Porosity evolution

The porosities of the as-deposited and isothermally heat-treated composite coatings are shown in Fig. 8. SEM images acquired from the polished cross sections were used to determine the porosity of the samples. The porosity results reported in this work were specifically from within the columns, as the contributions from the column gaps (inter-columnar regions) were excluded. All the pore sizes (small, large, elongated, etc.) were included in the measurements. Considering the uncertainty in the measurement, a comparable porosity was observed in the as-deposited and heat-treated (400 °C and 500 °C) composite coatings. However, the composite coating subjected to 600 °C exhibited a lower average porosity content than that of the as-deposited coating. It is reasonable to assume that the slight decrease in porosity observed after isothermal treatment at 600 °C can be related to the sintering of the YSZ matrix. Generally, sintering processes are performed at higher temperatures (above 1000 °C) to obtain highly dense YSZ coatings [47–49]. Hence, there is a lack of published literature on the exposure of SPS-processed YSZ coatings to 600 °C for a time duration of 8 h (exposure time used in this study). However, in the past, the onset of sintering of SPS-processed YSZ was reported to occur after 30 min at 800 °C, as measured using thermal conductivity measurements [50]. Sintering is a function of both temperature and time. Therefore, the suspension-derived YSZ microstructure resulting from sub-micron feedstock could have undergone accelerated sintering at an exposure temperature of 600 °C, resulting in the observed reduction in porosity. It should also be mentioned that no prior studies have used similar exposure test conditions (600 °C, 8 h duration), making it difficult to compare the results obtained in this study with those in the published literature. These differences in porosity can be observed in the SEM micrographs in

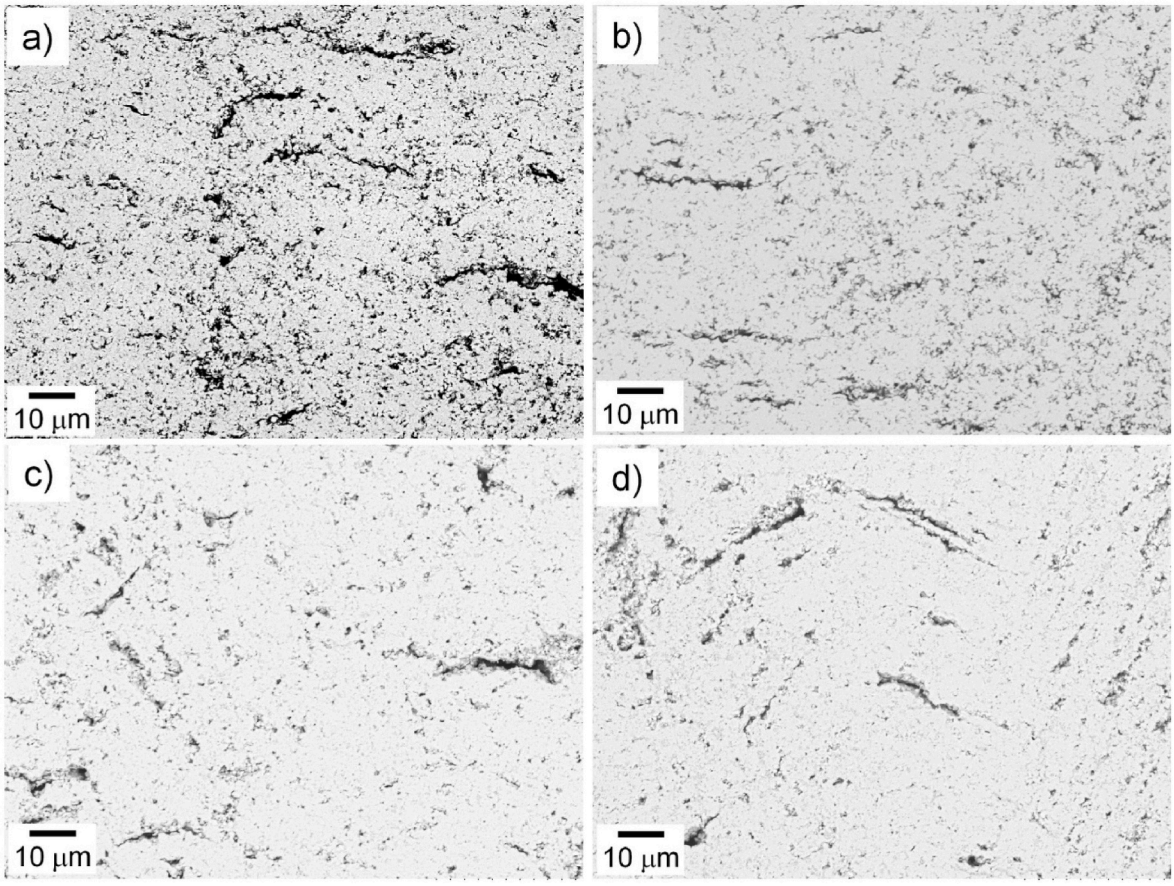

Fig. 9. Backscattered electron (BSE) micrographs of cross-sections of the YSZ-GNP coating in the as-deposited state (a) and after the heat treatment at 400 °C (b), 500 °C (c), and 600 °C (d).

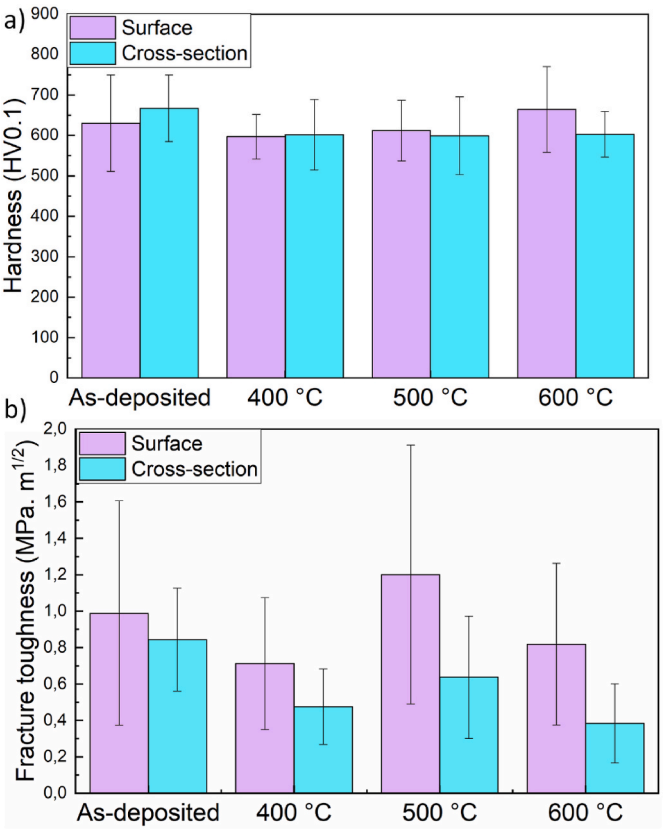

Fig. 10. Hardness (a) and fracture toughness (b) of the as-deposited and heat-treated YSZ-GNP coatings.

Fig. 9. In the 600 °C heat-treated specimens, large and elongated pores were retained after the heat treatment (see Fig. 9d), whereas the finer porosity observed in the as-deposited coating was reduced.

3.4. *Mechanical properties*

Similar to the porosity measurements, indents for the hardness and fracture toughness measurements were selectively made within the columns while avoiding column gaps in the columnar microstructured coatings. The hardness and fracture toughness values of the as-deposited and isothermally heat-treated composite coatings are shown in Fig. 10. Micrographs of the hardness indentations are provided in the Supplementary Information (see Fig. S1). Considering the intrinsic anisotropic microstructure of the coatings, the hardness was measured both from the surface and cross-section of the coatings, as shown in Fig. 10a. The results shown in Fig. 10a indicate that the hardness is comparable for all coatings, especially when considering the high scatter of the measurements. For all the coatings, a similar value of hardness was measured between the surface and the cross-section. This confirms that the coatings are characterized by comparable hardness. To consider the influence of the non-homogeneous distribution of the GNPs within the coatings, the fracture toughness was also measured from the surface and cross-sections of the coatings, and the results are shown in Fig. 10b. In addition, it should be highlighted that for the calculation of fracture toughness (see Eq. (1)) the cracks emerging in both horizontal and vertical directions from the indent vertices were used as a means to consider the effect of the different GNPs alignments within the YSZ columns. A representative micrograph of the indentation performed for toughness measurements is included in the Supplementary Information (see Fig. S2). As shown in Fig. 10b, the fracture toughness measurements performed on the cross-section and the surface show a high scatter in the data, which prevents an accurate ranking of the mechanical properties of the coatings. Typically, such high scatter in the fracture toughness measurement is often reported for suspension-sprayed YSZ coatings owing to their unique microstructural features such as different porosity classes (fine-scale porosity, coarse porosity), high number of splat boundaries, and finer splats [51,52]. Additionally, in this study, the incorporation of GNPs and their tendency to preferentially agglomerate at the column gaps further aggravated the microstructural inhomogeneity in the composite coatings. Based on the results observed in this study, it can be said that the microindentation analyses were inconclusive in ranking the mechanical properties of the investigated coatings. It should be mentioned that the fracture toughness evaluation of columnar coatings using other methods (e.g., three-point bending) poses different challenges, as column gaps tend to initiate fracture and predict the fracture toughness of coatings. Therefore, in future studies, a reliable evaluation of the mechanical properties of columnar GNP-reinforced coatings should be explored.

4. Summary and conclusions

In this study, YSZ-GNP composite coatings with a columnar microstructure were deposited using a suspension plasma spray (SPS) process with a mixed ethanol-based YSZ + GNP suspension. The microstructures of the composite coatings were studied using scanning electron microscopy (SEM) and Raman analyses, whereas the hardness and fracture toughness were measured by micro-indentation. Furthermore, the YSZ-GNP coatings were subjected to different isothermal treatments to study the thermal stability and evolution of the defectiveness of the GNPs in the composite coating. The following conclusions were drawn from the results of this study:

- SPS spraying using a mixed GNP-YSZ suspension is a suitable technique for depositing YSZ-GNP composite coatings with columnar microstructures.
- Raman mapping and point analysis confirmed the presence of GNPs with low defect density in the as-deposited composite. SEM analysis revealed that the GNPs were distributed along the cross-section of the coating, with GNPs mainly agglomerated along the inter-columnar spacing of the YSZ columns.
- The GNPs were preserved within the YSZ matrix, with a slight increase in their defect density after 8 h of isothermal treatment at 400 and 500 °C. However, after 8 h of heat treatment at 600 °C, an evident decrease in the number of GNPs was observed. Raman analysis revealed structural changes occurring in the GNPs at 600 °C, and the measured Raman spectra could be correlated to oxidized graphene.
- The as-deposited and heat-treated composite coatings were characterized by comparable porosities. A slight decrease in the average porosity content was observed in the composite coating heat treated at 600 °C, attributed to the sintering of the YSZ matrix.
- Considering the large scatter in the measurements, the hardness and fracture toughness of the as-deposited and heat-treated coatings were comparable. The observed scatter in the measurements can be related to the microstructural features of the columnar YSZ coatings and the observed GNP agglomeration.

The study results shown confirm that GNP-containing coatings can be successfully obtained using the SPS deposition route and that the microstructure of the deposited coating plays an important role in the distribution of GNPs. The ability to control the distribution of GNPs provides opportunities for thermally sprayed graphene-containing coatings to be used in various functional application.

Data availability

The raw/processed data required to reproduce these findings cannot be shared at this time as the data also forms part of an ongoing study.

Declaration of competing interest

The authors declare that they have no known competing financial interests or personal relationships that could have appeared to influence the work reported in this paper.

Acknowledgements

The authors would like to acknowledge the national Strategic Innovation Programme for graphene, SIO Grafen, for the financial support received. The programme is supported by the Swedish government agencies Vinnova (Sweden's Innovation Agency), the Swedish Energy Agency and the Swedish Research Council Formas. The project grant nr. Is Dnr 2018–03315.

Appendix A. Supplementary data

Supplementary data to this article can be found online at https://doi.org/10.1016/j.ceramint.2022.11.055.

References

[1] D.G. Papageorgiou, I.A. Kinloch, R.J. Young, Mechanical properties of graphene and graphene-based nanocomposites, Prog. Mater. Sci. 90 (2017) 75–127, https://doi.org/10.1016/J.PMATSCI.2017.07.004.

[2] S. Zhou, Y. Wu, W. Zhao, J. Yu, F. Jiang, Y. Wu, L. Ma, Designing reduced graphene oxide/zinc rich epoxy composite coatings for improving the anticorrosion performance of carbon steel substrate, Mater. Des. 169 (2019), 107694, https://doi.org/10.1016/j.matdes.2019.107694.

[3] J.H. Lee, S.J. Park, J.W. Choi, Electrical property of graphene and its application to electrochemical biosensing, Nanomaterials 9 (2019), https://doi.org/10.3390/nano9020297.

[4] E. Pop, V. Varshney, A.K. Roy, Thermal properties of graphene: fundamentals and applications, MRS Bull. 37 (2012) 1273–1281, https://doi.org/10.1557/mrs.2012.203.

[5] D. Berman, A. Erdemir, A.V. Sumant, Graphene: a new emerging lubricant, Mater. Today 17 (2014) 31–42, https://doi.org/10.1016/j.mattod.2013.12.003.

[6] X. Zheng, L. Gao, Q. Yao, Q. Li, M. Zhang, X. Xie, S. Qiao, G. Wang, T. Ma, Z. Di, J. Luo, X. Wang, Robust ultra-low-friction state of graphene via moiré superlattice confinement, Nat. Commun. 7 (2016), https://doi.org/10.1038/ncomms13204.

[7] K. Markandan, J.K. Chin, M.T.T. Tan, Recent progress in graphene based ceramic composites : a review. https://doi.org/10.1557/jmr.2016.390, 2016.

[8] H.G. Prashantha Kumar, M. Anthony Xavior, Graphene reinforced metal matrix composite (GRMMC): a review, Procedia Eng. 97 (2014) 1033–1040, https://doi.org/10.1016/J.PROENG.2014.12.381.

[9] J. Du, H.-M. Cheng, The fabrication, properties, and uses of graphene/polymer composites. https://doi.org/10.1002/macp.201200029, 2012.

[10] C. Lee, X. Wei, J.W. Kysar, J. Hone, Measurement of the elastic properties and intrisic strength of monolayer graphene, Science 321 (80) (2008) 385–388.

[11] L.S. Walker, V.R. Marotto, M.A. Rafiee, N. Koratkar, E.L. Corral, Toughening in graphene ceramic composites. https://doi.org/10.1021/nn200319d, 2011.

[12] J. Liu, H. Yan, M.J. Reece, K. Jiang, Toughening of zirconia/alumina composites by the addition of graphene platelets, J. Eur. Ceram. Soc. 32 (2012) 4185–4193, https://doi.org/10.1016/J.JEURCERAMSOC.2012.07.007.

[13] K. Wang, Y. Wang, Z. Fan, J. Yan, T. Wei, Preparation of graphene nanosheet/alumina composites by spark plasma sintering, Mater. Res. Bull. 46 (2011) 315–318, https://doi.org/10.1016/J.MATERRESBULL.2010.11.005.

[14] H.J. Kim, S.M. Lee, Y.S. Oh, Y.H. Yang, Y.S. Lim, D.H. Yoon, C. Lee, J.Y. Kim, R. S. Ruoff, Unoxidized graphene/alumina nanocomposite: fracture-and wear-resistance effects of graphene on alumina matrix, Sci. Rep. 4 (2014), https://doi.org/10.1038/srep05176.

[15] L. Kvetková, A. Duszová, P. Hvizdoš, J. Dusza, P. Kun, C. Balázsi, Fracture toughness and toughening mechanisms in graphene platelet reinforced Si3N4 composites, Scripta Mater. 66 (2012) 793–796, https://doi.org/10.1016/J.SCRIPTAMAT.2012.02.009.

[16] S.-M. Choi, H. Awaji, Nanocomposites-a new material design concept, Sci. Technol. Adv. Mater. 6 (2004) 2–10, https://doi.org/10.1016/j.stam.2004.06.002.

[17] P. Palmero, Structural ceramic nanocomposites: a review of properties and powders' synthesis methods, Nanomaterials 5 (2015) 656–696, https://doi.org/10.3390/nano5020656.

[18] M. Belmonte, C. Ramírez, J. González-Julián, J. Schneider, P. Miranzo, M.I. Osendi, The beneficial effect of graphene nanofillers on the tribological performance of ceramics, Carbon N. Y. 61 (2013) 431–435, https://doi.org/10.1016/j.carbon.2013.04.102.

[19] A. Nieto, L. Huang, Y.H. Han, J.M. Schoenung, Sintering behavior of spark plasma sintered alumina with graphene nanoplatelet reinforcement, Ceram. Int. 41 (2015) 5926–5936, https://doi.org/10.1016/j.ceramint.2015.01.027.

[20] A. Gallardo-López, I. Márquez-Abril, A. Morales-Rodríguez, A. Muñoz, R. Poyato, Dense graphene nanoplatelet/yttria tetragonal zirconia composites: processing, hardness and electrical conductivity, Ceram. Int. 43 (2017) 11743–11752, https://doi.org/10.1016/j.ceramint.2017.06.007.

[21] I. Ahmad, M. Islam, H.S. Abdo, T. Subhani, K.A. Khalil, A.A. Almajid, B. Yazdani, Y. Zhu, Toughening mechanisms and mechanical properties of graphene nanosheet-reinforced alumina, Mater. Des. 88 (2015) 1234–1243, https://doi.org/10.1016/J.MATDES.2015.09.125.

[22] A. Nieto, D. Lahiri, A. Agarwal, Synthesis and properties of bulk graphene nanoplatelets consolidated by spark plasma sintering, Carbon N. Y. 50 (2012) 4068–4077, https://doi.org/10.1016/j.carbon.2012.04.054.

[23] D.-T. Vu, Y.-H. Han, F. Chen, D. Jin, J.M. Schoenung, D.-Y. Lee, Graphene nanoplatelets reinforced ZrO2 consolidated by spark plasma sintering, Sci. Adv. Mater. 8 (2016) 312–317.

[24] A. Centeno, V.G. Rocha, B. Alonso, A. Fernández, C.F. Gutierrez-Gonzalez, R. Torrecillas, A. Zurutuza, Graphene for tough and electroconductive alumina ceramics, J. Eur. Ceram. Soc. 33 (2013) 3201–3210, https://doi.org/10.1016/J.JEURCERAMSOC.2013.07.007.

[25] S.M. Kwon, S.J. Lee, I.J. Shon, Enhanced properties of nanostructured ZrO2–graphene composites rapidly sintered via high-frequency induction heating, Ceram. Int. 41 (2015) 835–842, https://doi.org/10.1016/J.CERAMINT.2014.08.042.

[26] H.K. Jeong, Y.P. Lee, M.H. Jin, E.S. Kim, J.J. Bae, Y.H. Lee, Thermal stability of graphite oxide, Chem. Phys. Lett. 470 (2009) 255–258, https://doi.org/10.1016/j.cplett.2009.01.050.

[27] M.J. Nine, M.A. Cole, D.N.H. Tran, D. Losic, Graphene: a multipurpose material for protective coatings, J. Mater. Chem. A. 3 (2015) 12580–12602, https://doi.org/10.1039/c5ta01010a.

[28] D. Tejero-Martin, M. Rezvani Rad, A. McDonald, T. Hussain, Beyond traditional coatings: a review on thermal-sprayed functional and smart coatings, J. Therm. Spray Technol. 28 (2019) 598–644, https://doi.org/10.1007/s11666-019-00857-1.

[29] J.W. Murray, G.A. Rance, F. Xu, T. Hussain, Alumina-graphene nanocomposite coatings fabricated by suspension high velocity oxy-fuel thermal spraying for ultra-low-wear, J. Eur. Ceram. Soc. 38 (2018) 1819–1828, https://doi.org/10.1016/j.jeurceramsoc.2017.10.022.

[30] L. Liu, M. Qing, Y. Wang, S. Chen, Defects in graphene: generation, healing, and their effects on the properties of graphene: a review, J. Mater. Sci. Technol. 31 (2015) 599–606, https://doi.org/10.1016/J.JMST.2014.11.019.

[31] F. Venturi, J. Pulsford, T. Hussain, A novel approach to incorporate graphene nanoplatelets to Cr2O3 for low-wear coatings, Mater. Lett. 276 (2020), 128283, https://doi.org/10.1016/j.matlet.2020.128283.

[32] A. Ganvir, S. Björklund, Y. Yao, S.V.S.S. Vadali, U. Klement, S. Joshi, A facile approach to deposit graphenaceous composite coatings by suspension plasma spraying, Coatings 9 (2019) 1–6, https://doi.org/10.3390/coatings9030171.

[33] S. Mahade, A. Mulone, S. Björklund, U. Klement, S. Joshi, Novel suspension route to incorporate graphene nano-platelets in HVAF-sprayed Cr3C2–NiCr coatings for superior wear performance, J. Mater. Res. Technol. 13 (2021) 498–512, https://doi.org/10.1016/j.jmrt.2021.04.096.

[34] S. Mahade, N. Curry, S. Björklund, N. Markocsan, P. Nylén, R. Vaßen, Functional performance of Gd2Zr2O7/YSZ multi-layered thermal barrier coatings deposited by suspension plasma spray, Surf. Coating. Technol. 318 (2017) 208–216, https://doi.org/10.1016/J.SURFCOAT.2016.12.062.

[35] M. Shtein, I. Pri-Bar, M. Varenik, O. Regev, Characterization of graphene-nanoplatelets structure via thermogravimetry, Anal. Chem. 87 (2015) 4076–4080, https://doi.org/10.1021/acs.analchem.5b00228.

[36] S. Mahade, S. Björklund, S. Govindarajan, M. Olsson, S. Joshi, Novel wear resistant carbide-laden coatings deposited by powder-suspension hybrid plasma spray: characterization and testing, Surf. Coating. Technol. 399 (2020), 126147, https://doi.org/10.1016/j.surfcoat.2020.126147.

[37] A.G. Evans, E.A. Charles, Fracture toughness determinations by indentation, J. Am. Ceram. Soc. Discuss. Notes. (1976) 371–372.

[38] S. Mahade, A. Mulone, S. Björklund, U. Klement, S. Joshi, Incorporation of graphene nano platelets in suspension plasma sprayed alumina coatings for improved tribological properties, Appl. Surf. Sci. 570 (2021), 151227, https://doi.org/10.1016/J.APSUSC.2021.151227.

[39] K. Derelizade, F. Venturi, R.G. Wellman, A. Kholobysov, T. Hussain, Wear performance of graphene nano platelets incorporated WC-Co coatings deposited by hybrid high velocity oxy fuel thermal spray, Wear 482–483 (2021), 203974, https://doi.org/10.1016/j.wear.2021.203974.

[40] M.S. Dresselhaus, A. Jorio, M. Hofmann, G. Dresselhaus, R. Saito, Perspectives on carbon nanotubes and graphene Raman spectroscopy, Nano Lett. 10 (2010) 751–758, https://doi.org/10.1021/nl904286r.

[41] K. Derelizade, F. Venturi, R.G. Wellman, A. Khlobystov, T. Hussain, Structural changes of thermal sprayed graphene nano platelets film into amorphous carbon under sliding wear, Appl. Surf. Sci. 528 (2020), 146315, https://doi.org/10.1016/j.apsusc.2020.146315.

[42] B. Mukherjee, O.S. Asiq Rahman, A. Islam, M. Sribalaji, A.K. Keshri, Plasma sprayed carbon nanotube and graphene nanoplatelets reinforced alumina hybrid composite coating with outstanding toughness, J. Alloys Compd. 727 (2017) 658–670, https://doi.org/10.1016/j.jallcom.2017.08.160.

[43] P. Sokołowski, S. Kozerski, L. Pawłowski, A. Ambroziak, The key process parameters influencing formation of columnar microstructure in suspension plasma sprayed zirconia coatings, Surf. Coating. Technol. 260 (2014) 97–106, https://doi.org/10.1016/j.surfcoat.2014.08.078.

[44] K. VanEvery, M.J.M. Krane, R.W. Trice, H. Wang, W. Porter, M. Besser, D. Sordelet, J. Ilavsky, J. Almer, Column formation in suspension plasma-sprayed coatings and

resultant thermal properties, J. Therm. Spray Technol. 20 (2011) 817–828, https://doi.org/10.1007/s11666-011-9632-2.

[45] P. Sokołowski, L. Pawłowski, D. Dietrich, T. Lampke, D. Jech, Advanced microscopic study of suspension plasma-sprayed zirconia coatings with different microstructures, J. Therm. Spray Technol. 25 (2016) 94–104, https://doi.org/10.1007/s11666-015-0310-7.

[46] J. Ren, D. Zhao, F. Qi, W. Liu, Y. Chen, Heat and hydrothermal treatments on the microstructure evolution and mechanical properties of plasma sprayed hydroxyapatite coatings reinforced with graphene nanoplatelets, J. Mech. Behav. Biomed. Mater. 101 (2020), 103418, https://doi.org/10.1016/j.jmbbm.2019.103418.

[47] M. Yoshimura, Phase stability of zirconia, Am. Ceram. Soc. Bull. 67 (1988) 1950–1955.

[48] C. Laberty-Robert, F. Ansart, C. Deloget, M. Gaudon, A. Rousset, Dense yttria stabilized zirconia: sintering and microstructure, Ceram. Int. 29 (2003) 151–158, https://doi.org/10.1016/S0272-8842(02)00099-8.

[49] D. Hotza, D.E. García, R.H.R. Castro, Obtaining highly dense YSZ nanoceramics by pressureless, unassisted sintering, Int. Mater. Rev. 60 (2015) 353–375, https://doi.org/10.1179/1743280415Y.0000000005.

[50] S. Mahade, N. Curry, S. Björklund, N. Markocsan, P. Nylén, Thermal conductivity and thermal cyclic fatigue of multilayered Gd2Zr2O7/YSZ thermal barrier coatings processed by suspension plasma spray, Surf. Coating. Technol. 283 (2015) 329–336, https://doi.org/10.1016/j.surfcoat.2015.11.009.

[51] N. Curry, S. Mahade, A. Venkat, S. Joshi, Erosion performance of suspension plasma spray thermal barrier coatings — a comparison with state of art coatings, Surf. Coating. Technol. 437 (2022), 128311, https://doi.org/10.1016/J.SURFCOAT.2022.128311.

[52] D. Tejero-Martin, M. Bai, J. Mata, T. Hussain, Evolution of porosity in suspension thermal sprayed YSZ thermal barrier coatings through neutron scattering and image analysis techniques, J. Eur. Ceram. Soc. 41 (2021) 6035–6048, https://doi.org/10.1016/J.JEURCERAMSOC.2021.04.020.